Marwan Katurji [1]*, Jiawei Zhang [1], Ashley Satinsky[1], Hamish McNair [1], Benjamin Schumacher[1], Tara Strand[2], Andres Valencia[3], Mark Finney[4], Grant Pearce[2], Jessica Kerr[2], Daisuke Seto[1], Hugh Wallace[2], Peyman Zawar-Reza[1], Christina Dunker[6], Veronica Clifford[2], Katharine Melnik[2], Torben Grumstrup[4], Jason Forthofer [4], Craig Clements[5]

[1]University Center for Atmospheric Research, School of Earth and Environment, University of Canterbury, New Zealand;

[2]New Zealand Forest Research Institute, Scion, New Zealand

[3]Dept. Of Civil and Natural Resources Engineering, University of Canterbury, New Zealand;

[4]Forest Service, Missoula Fire Science Laboratory, United States of America

[5]Dept. of Meteorology and Climate Science, San Jose State University, United States of America

[6]Rocket Lab, New Zealand

*Correspondence author: Marwan Katurji (marwan.katurji@canterbury.ac.nz)

Key Points:

- High speed infrared cameras can be used for studying fire-atmosphere turbulent interactions
- Thermal Image Velocimetry/Image Segmentation methods can be employed to infer flaming zone kinematics to understand fire spread dynamics
- Turbulence derived from Thermal Image Velocimetry of flaming zone reveals similar spectral characteristics with atmospheric measurements

Abstract

We present novel in-field vegetation fire observations, and the analyses used to process the data, using brightness temperatures recorded by longwave infrared camera and thermal image velocimetry. The brightness temperatures from a wind-driven stubble wheat fire were obtained in video format with a 60 frames per second (fps) acquisition rate. Multi-level sonic anemometers mounted on a 10m in-fire tower were used for in-situ measurements of turbulent velocity and air temperatures, while fuel level air and flame temperatures were collected by an array of thermocouples. The camera's image pixel resolution was adequate to resolve dynamics and in accordance with the in-fire thermocouple spacing distances. The in-situ and remotely measured flaming zone dynamics were derived using two different methodologies, Thermal Image Velocimetry (TIV) and Image Segmentation (IS). The results highlight spatial and spectral information of coherent turbulent and mean velocity structures. The power spectra decomposition of the thermal image velocimetry showed similar spectral characteristics to the sonic velocity measurements during the fire passage under the tower with

a similar inertial subrange slope. This result reveals plausible evidence of interaction between the flaming zone and wind turbulence for a prescribed rapidly moving stubble wheat fire. This research presents a new field measurement methodology for understanding fire-atmospheric interactions between the flaming zone and the immediate overlying atmospheric turbulent boundary layer.

**Plain Language Summary**

The size and destructive power of wildfires can vary depending on weather and fuel conditions. We have carried out wheat stubble burning experiments using specialized instrumentation in order to study how the wind and fire interact, and the subsequent role of this interaction in the development of a wildfire. We used Long-Wave InfraRed or LWIR cameras to capture radiation emitted by the fire but invisible to the human eye. We then used the time-sequenced LWIR images to detect and calculate forward motion and fluctuation of the fire. We demonstrated for the first time the validity of these techniques by comparing the results with wind measurements collected during the passage of the fire using sonic anemometers. This new observation method has provided the first set of two-dimensional observations of the interaction between the flame zone and the overlying wind.

## 1 Introduction

A wildfire is a complex, multi-scale, and multi-process dynamical system with its instantaneous state depending on chemical and physical processes occurring on a hierarchy of spatial and temporal scales. Observations of multiscale processes affecting the wildfire are very difficult to make. These scales are as small as fuel particles during the combustion process (order of <10cm), flame structures and heat transfer (order of one to tens of meters), and microscale/mesoscale meteorological processes (orders of 10m to 10000m) (Morvan, 2011; Sullivan, 2017a, 2017b). As point measurements, micrometeorological in-situ towers in experimental burns provide spatially limited information over a brief period of time as the fire approaches and then travels underneath the instrumented tower (Clements et al., 2007, 2008; Heilman et al., 2019; Seto et al., 2013, 2014). This observational approach, while providing information on the quasi-stationary exchange of turbulent heat and momentum between the fire front and overlying atmosphere, does not capture the instantaneous spatial interaction between the flaming zone (defined by the wind and buoyancy driven visible flames) and the overlying atmospheric turbulence regime.

An observation method that can provide spatial observations of turbulent velocity within the flaming zone at field scale applications will elucidate the role of convection in fire spread. Earlier attempts of spatially distributed temperature measurements have showed additional observational advantages, however the fibre optic cable used in these experiments proved challenging to deploy in vegetation (Cram et al., 2016; Tangney et al., 2018). Aerial and satellite-based infrared remote sensing for spatially distributed temperature measurements can help in the detection and monitoring of wildfires, and have been largely employed

for operational fire management (Hua & Shao, 2017; Mazzeo et al., 2007), however resolution is too large to discern the convection physics at the fire front.

In previous fire behavior studies, the use of near-target Long Wave InfraRed (LWIR) imagery with other spectral imaging techniques was used to understand the relationship between fuel spatial variability and characteristics, fuel consumption, and smouldering and flaming processes with the fire's emitted radiative heat flux (Hudak et al., 2016; McRae et al., 2005). In these efforts, the challenge was calibrating for accurate brightness temperature (hereafter referred to as Tb) based upon image geo-referencing and ortho-rectification, and removing wind-induced camera movements (O'Brien et al., 2016). In addition, selecting the correct target emissivity values is problematic as they can vary between 0.1 and 0.9 depending on flame thickness and mixture of soot and combustible gas (Boulet et al., 2011; Johnston et al., 2014). Despite the availability of research grade LWIR cameras that are capable of high frame rates (exceeding 100 frames per second; fps), their use in experimental fires to study spatial and temporal flow dynamics within and around the fire are hereto limited.

For wildfire applications, Coen et al. (2004) and Clark et al. (1999) used a 30 and 60fps mid-wave infrared camera to calculate hot-plume vertical advection velocity based on time sequential velocimetry analysis of brightness temperature patterns. The images were taken from the side and front of a crown fire to derive hot plume vertical and along sloping terrain advection velocities. They observed new crown fire spread dynamics where local fire-induced bursts of heat emerged from the canopy crown to aid the spread of the fire. In other disciplines, such as micrometeorology, high speed infrared cameras were used to derive the velocity of coherent temperature structures and study their impacts on the energy and moisture exchange between the surface and overlying atmosphere (Garai & Kleissl, 2013; Inagaki et al., 2013; Katurji et al., 2013; Schumacher et al., 2019). High frame rate LWIR cameras have been used with the development of new velocimetry methods suitable for characterizing atmospheric turbulence. One such method is Thermal Image Velocimetry (TIV), which tracks the movement of thermal footprints using time sequenced image correlation techniques. In non-fire applications, the TIV method was used to visualise airflow over artificial surface types like polystyrene boards and turf (Inagaki et al., 2013). This was then validated against numerical simulations and in-situ field measurements (Schumacher et al., 2019).

In this work, we demonstrate that the derivation of advection velocity using TIV from high frame rate LWIR is suitable for observing fire-atmospheric interactions at the intermediate scale between the flaming zone and the overlying atmospheric turbulence boundary layer. We used a high frame rate (60 fps) LWIR camera to observe a rapidly advancing flaming zone front associated with an experimental stubble wheat burn. Advection velocity was derived from the observed thermal patterns using TIV. We present a description of our TIV method for tracking thermal patterns over a fire front. The TIV results are then compared to an independent velocimetry technique based on Image Segmenta-

tion (IS) to validate the method. This is then followed by the experimental set up, description of observations, and the use of the TIV with traditional in-fire and tower-based temperature and wind velocity point measurements. Finally, we compare the derived advection speeds of flame parcels from within the flaming zone to the overlying atmospheric turbulence, and then discuss the potential coupling of atmospheric driven coherent turbulence structures to flame dynamics.

## 2 Description of Techniques

### 2.1 Thermal Image Velocimetry

The Thermal Image Velocimetry (or TIV) method tracks the surface movement of thermal patterns measured by a LWIR camera using time sequenced image correlation techniques (Inagaki et al., 2013; Schumacher et al., 2019). The algorithm converts the time sequenced images into a spatiotemporally resolved velocity field at the camera's pixel resolution and sampling frame rate. The method involves maximizing the correlation between time and space window filters for individual pixels while going through all the image pixels at two consecutive time steps. Within a fire, the Tb (brightness temperature) of the flaming zone is an order of magnitude greater than its surroundings, including the smouldering ground or the reflectance from instrumentation (Figure 1). This minimizes the noise inside the flaming zone and allows for high quality analyses on thermal advection speed of the flaming zone. The thermal image velocimetry algorithm is continuously under development and an updated copy is freely available from Schumacher (2021).

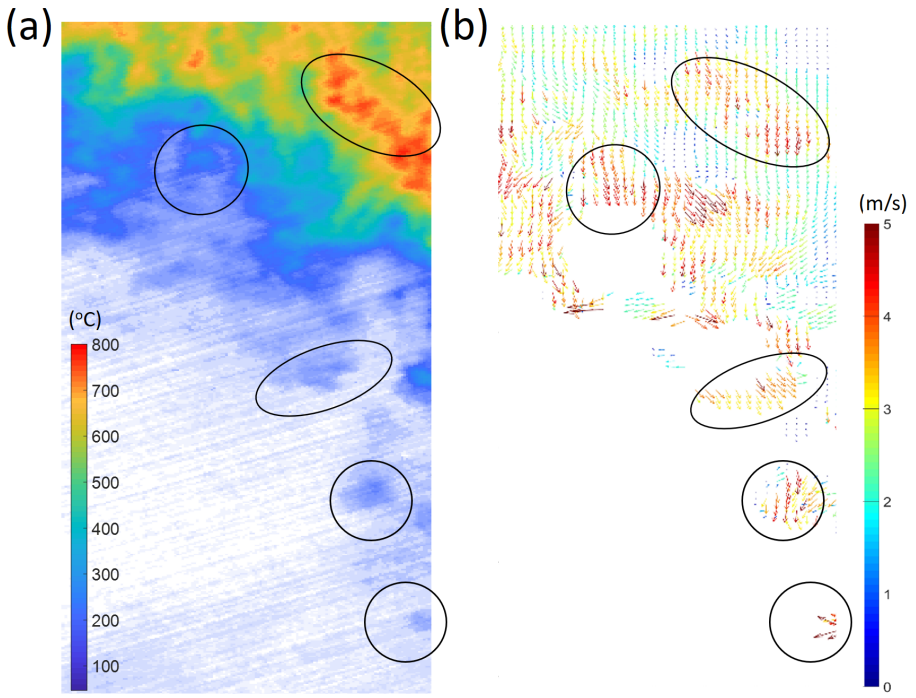


**Figure 1.** **(a)** A sample of the Tb measured by the LWIR camera showing the fire's flaming zone propagating from the top to the bottom of the image. **(b)** The resulting thermal advection velocity calculated using the TIV technique applied to the full range of the detected Tb values. The black circles represent locational references for both panels.

2.2 Image Segmentation

Image Segmentation (IS) methodology is a computer vision processing technique that allows for the identification and placement of pixels into labelled groups that share similar characteristics. IS was used to track flame parcels (defined here as clusters of hot temperature anomalies within the flaming zone), study their kinematic properties and cross-validate the TIV results. The flame parcel identification and tracking method is based on the watershed image segmentation process (Najman & Schmitt, 1994). This well-known image segmentation algorithm has been used to characterise particulate matter in nanomaterial observed by electron microscopy (De Temmerman et al., 2014) and in the analyses of magnetic resonance brain images (Beare et al., 2013).

To identify the flame parcels and to remove the data that represented smoke (lower temperature) a temperature-based distribution filter was first applied on the recorded time-sequenced Tb images. The $90^{th}$, $95^{th}$ and $98^{th}$ temperature distribution threshold filters were tested and the $98^{th}$ percentile threshold was best suited for tracking and computing thermal velocity advection (Figure 2).

This threshold filter highlighted the flaming zone area while reducing the noise incurred from smoke.

Threshold processing was then used to produce a binary image that shows only the fire front (Figure 2f). Subsequently, watershed segmentation was applied to the binary image to enable identification of "local maxima" or the non-null pixels in the binary images (Figures 2g and 2h). It also identified the pixels farthest away from the null pixels (black in Figures 2f) and it located potential flame parcels based upon regions defined by local maxima (Figures 2h).

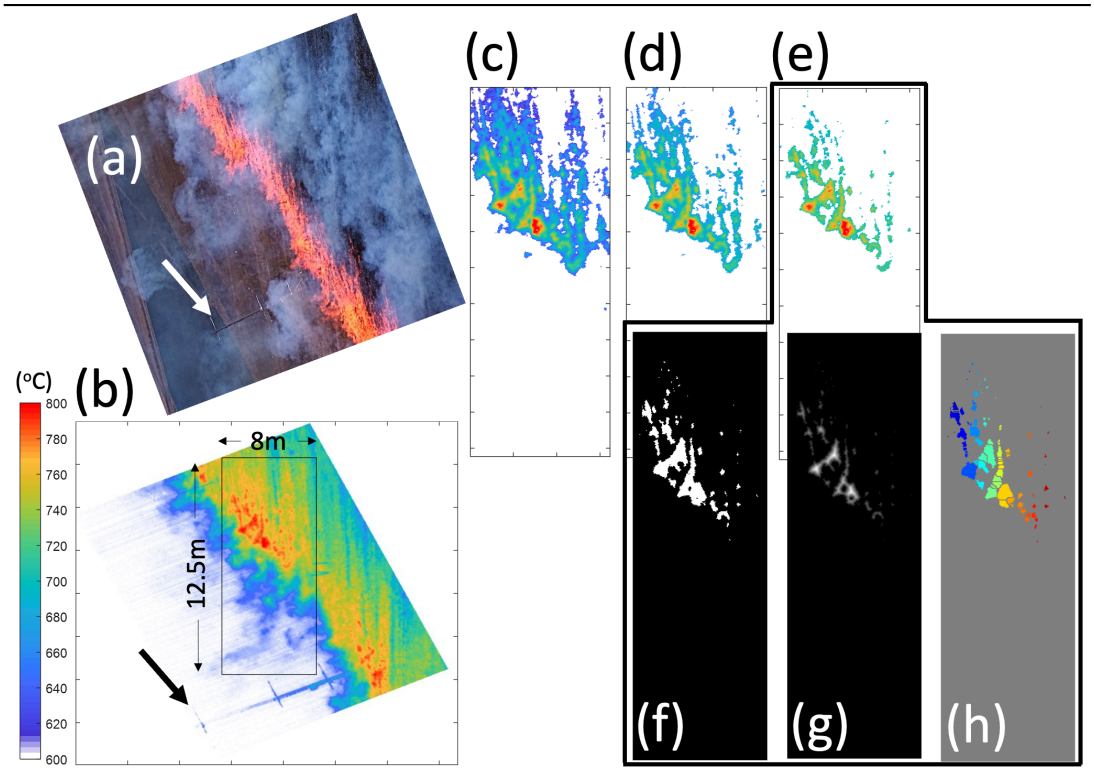


**Figure 2.** **(a)** Visible image taken from the elevated platform showing the approximate field of view of the infrared camera as shown in (b), the white and black arrows mark the 10m in-fire turbulence tower. An overhead view from an unmanned aerial vehicle is shown in the supplementary material ***video_S1.mp4***; **(b)** Brightness Temperature, Tb, for the entire field of view and temperature range from the infrared camera, the black and white arrow marks the 10m in-fire turbulence tower and a black box outlines the Image Segmentation (IS) analysis area; **(c)**, **(d)**, and **(e)** show the temperature distribution after application of IS filtering for the $90^{th}$, $95^{th}$, and $98^{th}$ percentiles respectively. An animation of (c) is provided in supplementary

material ***video_S2.mp4***; **(f)** a binary, white/black, processed image of (e); **(g)** the distance transform applied on binary segmented image; **(h)** the resulting segmented watersheds outlining the detected flame parcels. The temperature color legend in (b) only applies to (b), (c), (d) and (e).

The IS method allowed for segmenting, identifying and tracking potential flame parcels across multiple consecutive frames, as well as for computing their trajectory and advection velocity. After a careful consideration of outliers only potential flame parcels meeting the following assumptions were considered:

1. Flame parcels have to contain a minimum of 5 pixels that are greater than 750°C, to properly aggregate groups of pixels that do not represent individual flamelets.
2. To reduce outliers associated with flame flickering in and out of pixels, flame parcels cannot exceed an advection speed of 30m $s^{-1}$, and only parcels moving in both the streamwise and crosswise directions were considered.

Defining flame parcels in this manner allowed for a unique and clear identifier to be assigned to each parcel that enabled continuous spatial-temporal monitoring. Tracking individual parcels allowed for new spatial-kinematic information, such as thermal advection speed, to be derived.

## 3 Experiments and Methods

### 3.1. Experimental set-up

Twelve experimental research burns were carried out in Darfield, New Zealand during March 2018 (Figure 3 shows 11 out of 12 experimental zones). A comprehensive in-situ and remote sensing instrumentation package was set up to measure atmospheric and fire turbulence dynamics. The experimental design aimed to capture data from across a range of turbulent scales, extending from equivalent fuel size to several hundred meters into the ABL. Specifically, observations occurred at the fuel particle size (order of <10cm), flame structure and heat transfer size (order of 1 to tens of meters), and microscale/mesoscale size (orders of 10m to 10,000m). A detailed description of the experimental design and instrument specifications is available from Finney et al. (2018). A subset of experimental burns, EE1 and EE3 carried out on March 11, 2018, and observations (Table 1 and Figure 3) were used for these analyses.

Infrared image measurements were acquired using a Telops cooled FAST-IR L200 LWIR camera capable of 234 fps in full 640x512 pixels and 17200 fps in sub-windows. The camera was operated in the longwave band between 7.7 m to 9.3 m with a 50mm narrow angle lens to reduce lens distortion effects and resolve smaller features and was factory calibrated for an extended temperature range up to 1500°C). The effective pixel resolution of approximately 5 cm was calculated by counting pixels of known targets such as the meteorological tower and flame height measuring poles visible in the camera's field of view.

The camera was located 20 m above ground level and had a full view of the

fire's flaming zone and was set to acquire at 60 fps to best match the acquisition rates of the in-situ thermocouples, which collected data at 50 Hz, and wind sonic anemometers, which subsampled data to 20Hz. To further reduce any lens distortion effects, we have limited our analyses to a central window of 8m by 12m (Figure 2b). The sonic anemometers (K-type and Vx-type, ATI, Boulder Colorado) were mounted on a 10m in-fire tower located at the center of each burn plot at 1.6m, 5m, and 10m above ground level (AGL). A horizontal array of thermocouples (custom made, Missoula Fire lab, Missoula Montana) were positioned on the fuel bed and perpendicular to the fire-front.

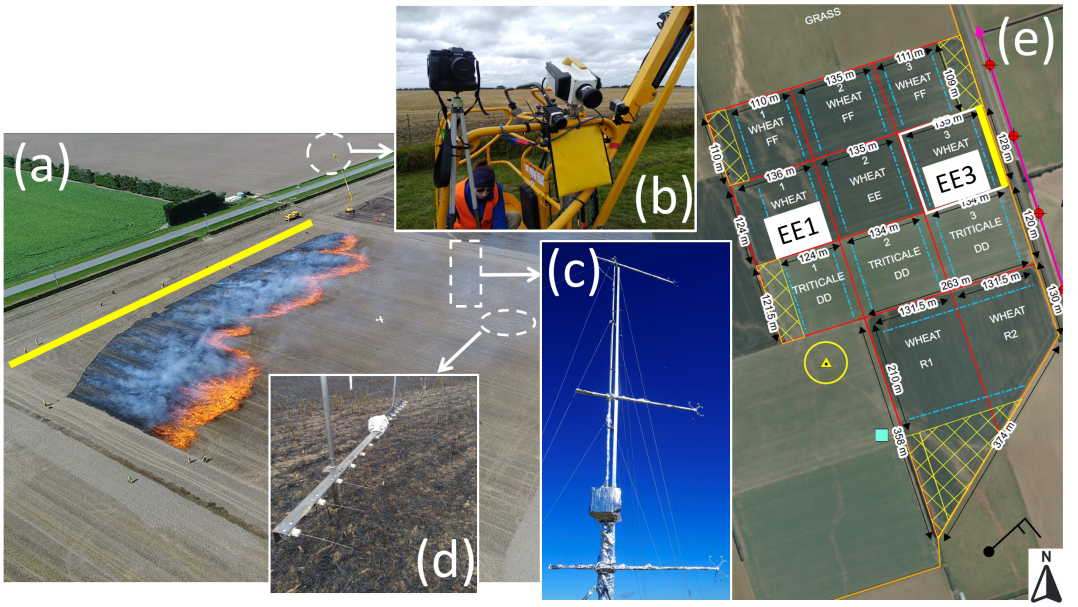


**Figure 3.** Experimental burn layout. **(a)** Picture from an unmanned aerial vehicle showing the fire front progression (the thick yellow line is for reference in (e); **(b)** The infrared camera (shown in the white casing) is located on a 20m high elevated platform and marked with a dashed white circle in (a); **(c)** the 10m in-fire sonic anemometer tower inside the dashed white rectangle of (a) with three sonic anemometers installed on cross arms along with a vertical array of 20 thermocouples; **(d)** a section of the horizontal fuel-level thermocouple array showing 16 thermocouples at 15 cm spacing inside the dashed oval; **(e)** layout of all experimental burn plots, including the two cases EE1 and EE3, carried out in the NZ-Fire experiment with their dimensions and fuel types. The wind barb at the bottom right of the panel shows the mean wind speed and direction during EE1 and EE3 experiment. The yellow thick lines are inserted in (a) and (e) for reader orientation reference.

**Table 1.** *Experimental conditions and observational system details. General meteorological conditions recorded at the site from 10m Above Ground Level (AGL) from a standard AWS at the site.*

| Exp. | Air temperature [°C], relative humidity [%] | Wind speed [$ms^{-1}$] and direction [°] for 10r |
|---|---|---|
| EE1 | 15, 70 | 6.5, 35 |
| EE3 | 19, 62 | 8.8, 47 |

**Table 2.** *Observational systems used in the experiments and corresponding measurement parameters and specifications.*

| Observational System | Instrument | Accuracy, range (sensitivity, resolution) | Measured variable | Installation details |
|---|---|---|---|---|
| Time sequential Long Wave Infrared (LWIR) imaging | Telops L200 50mm lens 7.7µm to 9.3µm | ± 1°C, 100 to 1500°C (0.022°C, ~5cm/px) | Brightness temperature (Tb) 60fps, 640x512 px | On elevated platform, 20m AGL. Oblique field of view of the fire line and flaming zone |
| In-fire wind turbulence tower | Applied Technologies, Inc. 3-dimensional ultrasonic anemometer – SATI/3(K) series, Campbell Scientific CR6 datalogger | K-probe - 150 mm vertical and horizontal measurement path length. Sample frequency 20Hz | U (+ve towards east), V (+ve towards north), W (+ve vertically upwards) [$ms^{-1}$] | 1.6m (6h, 6.4h), 5m (18.9h, 20h), and 10m (37.7h, 40h) AGL and perpendicular to fire line |
| Horizontal thermocouple array | Type K thermocouple | ± 2°C, -200 to 1260°C (41 V/°C, 0.1°C) | Air/gas temperature [°C] | thermocouples at 15cm spacing, perpendicular to fire line, and at fuel height level |

3.2. Research burns conditions

Special attention was given to produce a steady state fire line with negligible edge-effects at the center of the burn. Evidence of negligible edge-effects at the centre of the fire-front is a fire-front that appears nearly as a straight line (i.e., Figure 2a). To obtain this straight line careful consideration was given to the size of the burn plot and ignition method of the fire to counteract the natural tendency for elliptical propagation. The in-situ ground instrumentation were located at the centre of the fire line to mitigate influence of the edges on the data.

All research burns were carried out on flat terrain and burns EE1 and EE3 occurred in wheat stubble with canopy height and fuel moisture contents and loadings as described in Table 1. Although their fuel types were similar, the time of ignition, morning (EE1) and afternoon (EE3) led to different meteorological conditions and stalk and litter fuel moisture contents. The average fire spread rates reflect these differences with EE1 spreading at 0.68m $s^{-1}$ under lighter wind speeds and elevated fuel moisture contents and EE3 spreading at 1.08m $s^{-1}$. These average spread rates were estimated based on aerial video footage. Fire spread rate was also calculated from the horizontal thermocouple arrays using cross-lagged correlations of air temperature from the 32 thermocouples (see Table 1). The values are similar at 0.8m $s^{-1}$ for EE1 and 1.5m $s^{-1}$ for EE3 (Finney et al., 2018). The prevailing wind direction was from the northeast sector for all experimental burns and referenced by the wind barb (for reference in Figure 3e).

### 3.3. Data processing

#### 3.3.1 Infrared image stabilization

Video stabilization of the acquired infrared images was carried out first, which eliminated the impact of wind-induced oscillations on the camera while on the elevated platform. The stabilization was applied using the motion tracking functions of the open source software Blender (Community, 2018; Hess, 2013). Low emissivity stationary targets for video stabilization were used from image to image to stabilise the video. The stationary targets included the 10m in-fire turbulence tower made of steel and visible in low magnitude Tb and in-fire camera boxes wrapped in highly reflective heat shielding. Both increased in LWIR visibility as the fire front travelled through the instrumentation and were therefore visible in the camera video with and without fire. The Blender stabilization algorithm requires color value pixels. Therefore, to stabilize the infrared footage we converted the unstable infrared video to RGB color. Then the RGB color video was stabilized and subsequently returned into Tb 3-dimensional data cubes (x,y, time) using a vector quantization method with the color values in a look-up table. This method was subsequently improved using a random forest machine-learning model (Schumacher et al., 2019) to increase the accuracy of Tb retrieved from color value pixels.

#### 3.3.2 Sonic anemometer data treatment

Time series data from the sonic anemometers were processed to remove unreal-

istic spikes using the de-spiking routine proposed by Vickers and Mahrt (1997). Data spikes during the research burn that were larger than 3.6 times the standard deviation within a 1 minute moving average window were replaced by linearly interpolated values. We chose ± 3.6 standard deviations due to the lower intensity nature of our burns, based on Seto et al. (2014), Clark et al. (1999) and Coen et al. (2004). The data were then checked for any sensor tilt effects by tilt correcting using the planar fit method (Wilczak et al., 2001). The root mean square deviations before and after the corrections were calculated for the duration of the burn, and were only 0.3m $s^{-1}$ for vertical velocity and 0.7m $s^{-1}$ for horizontal wind speed. The calculated spectra before and after the tilt correction were not affected by this correction process.

## 4 Results

### 4.1. General observation of the fire front characteristics

A visual inspection of the image-time sequence of EE1 and EE3 fire fronts along with the fuel-level thermocouple readings for both experiments shows a deeper flaming zone for EE3 (Figure 4). Quantitatively, the flaming zone depth is represented by the variability in the 50 Hz and 1-min average temperature (Figures 4b and 4d). Both meteorological and fuel moisture conditions contributed to EE3's greater flaming depth with drier fuel conditions and higher wind speeds as compared to EE1 (Table 1). Flame height, measured using calibrated in-fire poles painted black and white at 0.5m intervals, was approximately 1m AGL (3.8h, EE1) and 2m AGL (8h, EE3), where h is the mean fuel height.

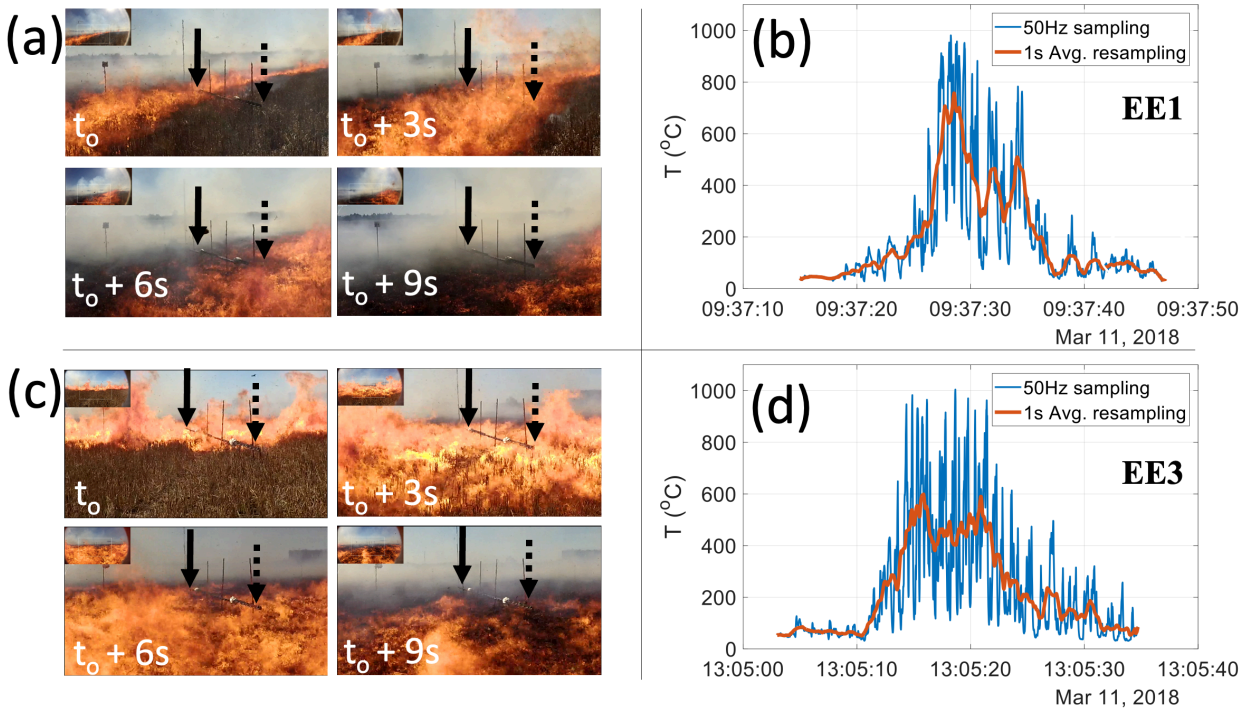


**Figure 4.** Fire front passage as viewed by an in-fire camera for (a) EE1 and (c) EE3 relative to the horizontal thermocouple array, which is marked at its endpoints by the black solid and dotted arrows. The four picture insets in (a) and (c) show a 3s time lapse set of images on the horizontal thermocouple array that measured temperature (b) and (d) as the fire front passed through, shown as a time series from the first thermocouple. Blue and red lines show the 50Hz and 1s average data respectively.

4.2. Evaluation of the spatiotemporal suitability of high-speed LWIR for in-fire temperature observations

Comparing LWIR images with a time-series from a single pixel (sampled at 60fps) of the Tb demonstrates the wealth of data this method collects (Figure 5). Time series from a single pixel matched with the LWIR images shows influence of smoke/hot combustible gases crossing the pixel, followed by the fire front passage through the pixel and then a linear cooling as slow infrared energy was release from the hot ground.

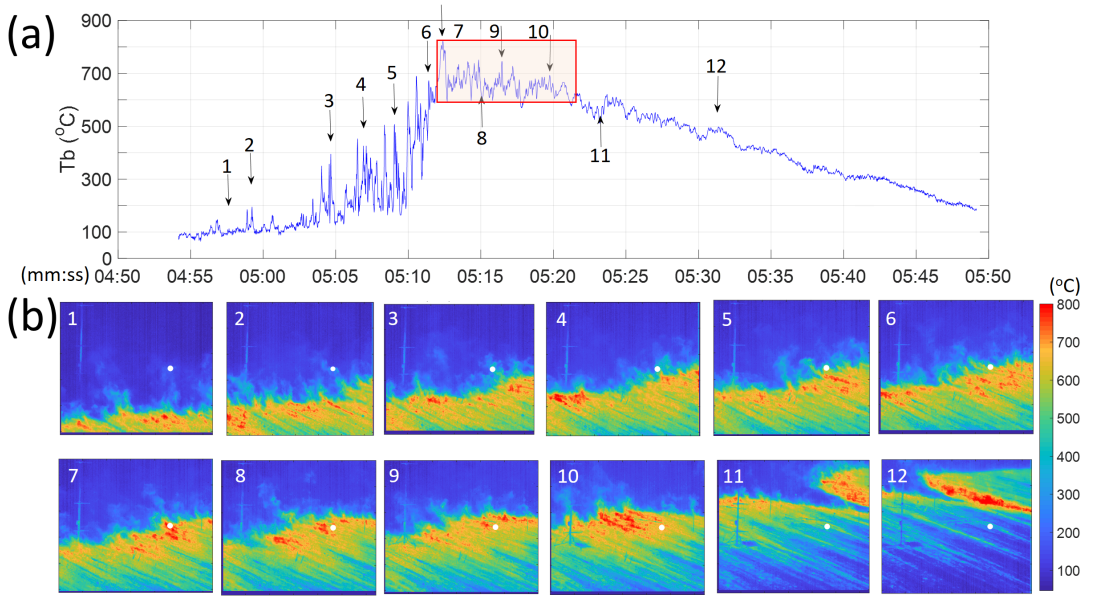


**Figure 5.** Brightness temperature (Tb) point and image series from EE3 as the fire front was crossing the in-fire wind turbulence tower: **(a)** time series of Tb taken from the white dot location marked in (b). The annotated arrows point to the periods represented in the Tb images in (b) while the red box represent the flaming zone period; **(b)** Tb images taken by the infrared camera.

The data from the horizontal in-situ fuel-level thermocouple (TC) array was used to validate the Tb data. The objective of this comparison was to evaluate the suitability of the LWIR camera's pixel resolution in terms of resolving brightness temperature changes across the thermocouple array. In both EE1 and EE3, 32-pixel locations from the time-sequenced Tb images that aligned with the thermocouple locations were extracted for analyses. Autocorrelations between thermocouples were used to build a curve for comparison against autocorrelations between pixels (Tb) for the same spatial location (Figure 6). These curves demonstrate the lag time of exposure to the fire front between 8 horizontal distances that ranged from 0.15m (T1 to T2) to 1.05m (T1 to T8).

This analysis was done to verify that the sampling rate and spatial resolution of the LWIR camera was able to detect the temperature changes as observed by the TC array. Both systems show similar lag periods (Figure 6b and 6c) verifying the capability of the LWIR camera to sense the thermal and dynamic shifts due to fire front passage.

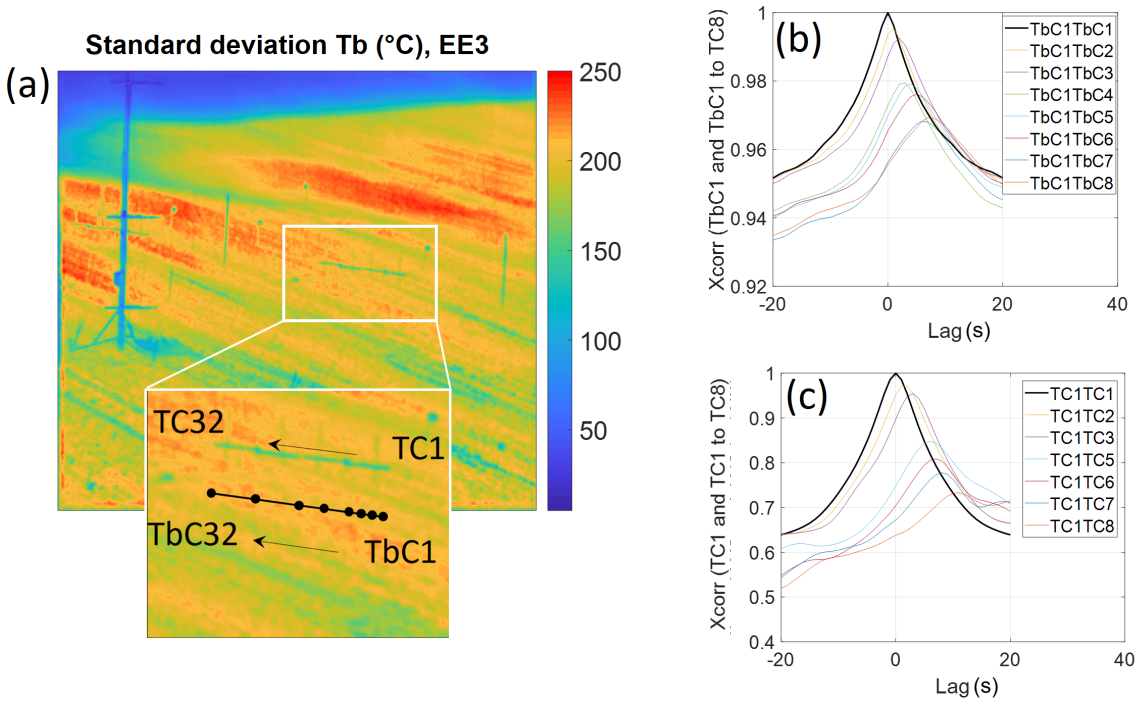


**Figure 6.** Cross correlations between the temperature measurements of the horizontal thermocouple array and the nearby Tb pixels. (a) Temporal standard deviation of each pixel in the infrared image with an enlarged view of the thermocouple array viewed in infrared. TC1 to TC32 represent the thermocouple temperature measurements and TbC1 to TbC32 represent the equivalent Tb measurements (virtually represented by balck dots); (b) and (c) cross correlations between TC and Tb for the first 8 thermocouple measurements of the EE3 case.

4.3 Comparison of two methods for computing mean advection speed

The TIV and IS were two different methods used to compute the mean advection speed of the hot parcels of air within and near the flaming zone. The results from both methods show similar trends and magnitudes (Figures 7a and 7b). The comparison period covers the fire front passage through the analysis area, as shown in Figure 2b, and the advection speeds were spatially averaged at each image sequence. Both independent methodologies consistently produced a similar mean advection speed throughout the fire front passage for both research burns. This cross evaluation gives confidence in the LWIR technique for use in computing mean advection speeds near and within the fire front. The IS is an independent method with different spatiotemporal filters and scales as compared to the TIV. TIV is the preferred method for observing in-situ turbulence because

it preserves the high frequency temporal fluctuations of the signal.

The mean advection speeds of flaming zone from the TIV method for EE1 and EE3 were 3.7m $s^{-1}$ and 5.3m $s^{-1}$, respectively. The difference (EE1 lower than EE3) likely relates to both the differences in the overlying wind speeds, 6.5m $s^{-1}$ and 8.8ms $^{-1}$ at 10m AGL for EE1 and EE3, respectively.

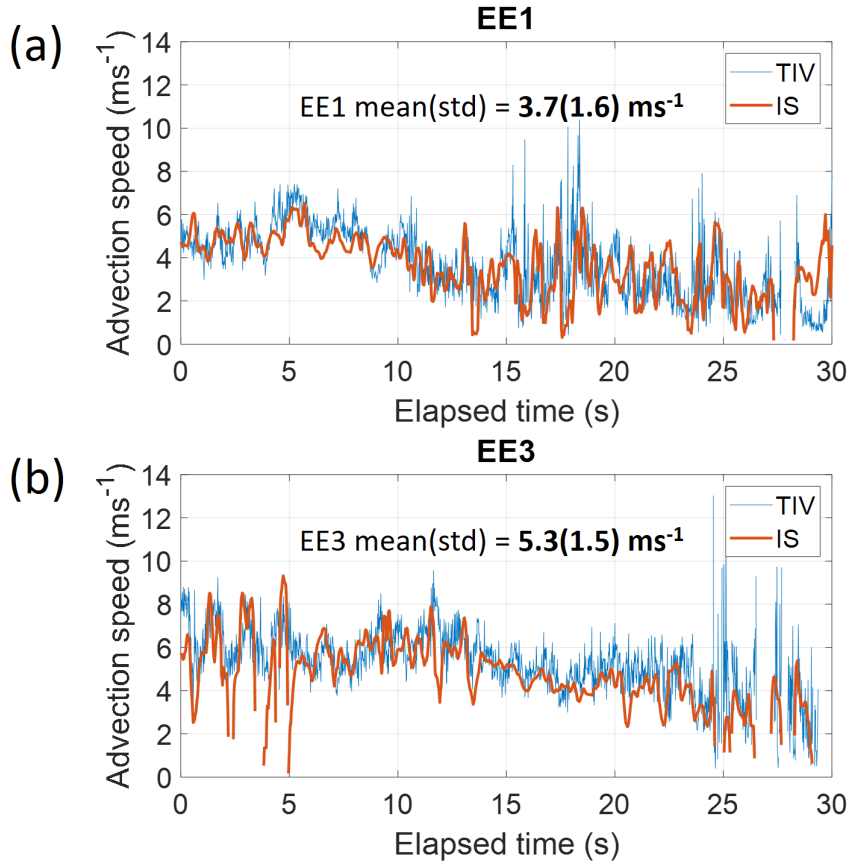


**Figure 7.** Advection speeds of the flaming zone (temporal standard deviation) calculated with two different methods and for the (a) EE1 and (b) EE3 experimental cases. The methods are the Thermal Image Velocimetry (TIV, thin blue line) and Image Segmentation (IS, red line). The mean and standard deviation (std) are from the TIV method.

4.3 Comparison of TIV-based wind speed distribution and turbulence spectra

The wind speed measured at 10m AGL was higher than both the wind speed measured at 1.6m and the TIV spatially averaged advection speed for EE3

(Figure 8a). To aid with visual inspection a shift of the 1.6m wind speed values to match the peak of the distribution of TIV advection speeds (see dotted blue line in Figure 8a) reveals that the shape of the TIV advection speed distribution matches the distribution of the computed vector wind speed from the 1.6m sonic, although peaks differ.

To identify and compare the frequency information of the TIV derived advection speeds with the overlying wind turbulence, we applied a Fast Fourier Transform (FFT) decomposition using the p-Welch method (Welch, 1967) on both TIV and the 1.6m and 10m sonic datasets (Figure 8b). The speed perturbations were derived from a mean window of 2-seconds and the data used for the FFT was at 20Hz for the tower-based wind speeds and 60Hz for the TIV-based advection speeds. The results show matching spectral peaks at around 0.6Hz and similar high frequency slopes up to 10Hz with all data following the expected turbulent inertial subrange empirical -5/3$^{rd}$ slope (Stull, 2012).

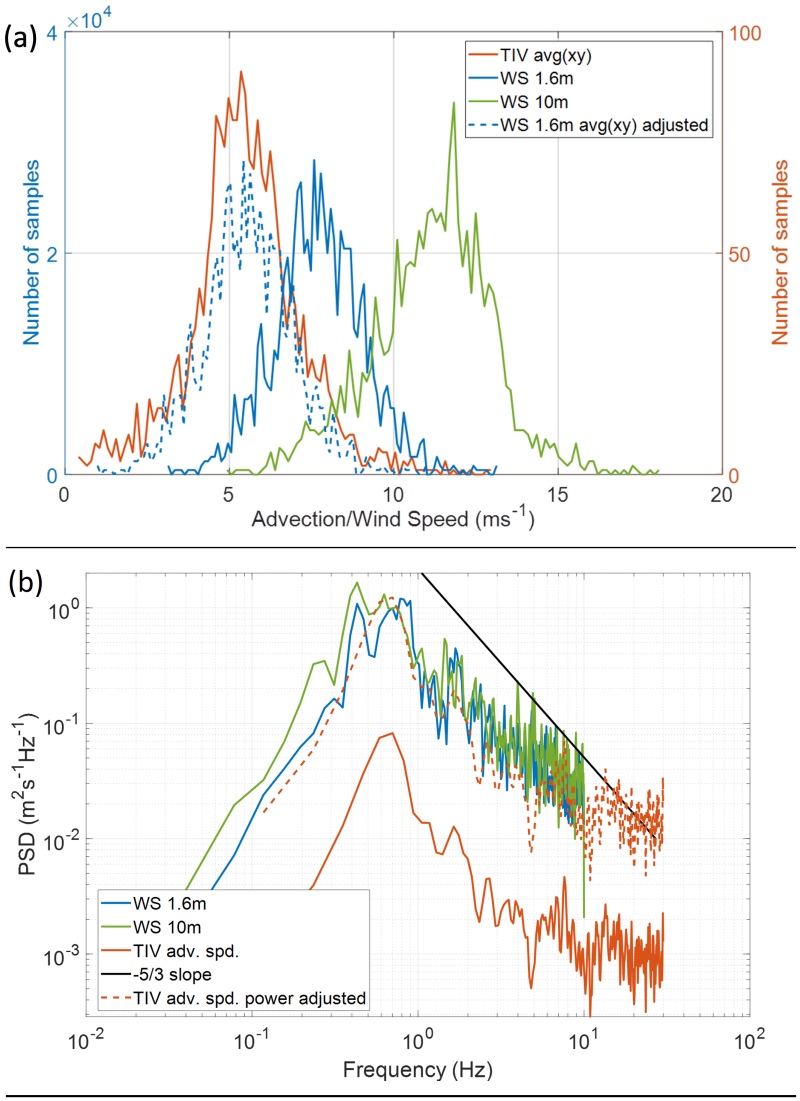


**Figure 8.** (a) Number distribution of the total TIV advection speed values for EE3 (TIV avg(xy) for spatially averaged advection speed within the sampled region at each time step). Wind speed was computed from the data recorded by the sonics located at 1.6m and 10m AGL and not from the AWS data used in Table 1 for general meteorological conditions. For visual inspection of the profile, the dotted blue line represents the adjusted distribution of WS 1.6m by shifting the blue line to the left to match the peak with the TIV avg(xy) distribution. (b) The Power Spectral Density (PSD) derived by applying the Fast Fourier Transform (FFT) on the calculated perturbation fields of the TIV

advection speed and the wind speed measured at the two sonic anemometer height levels. The TIV power adjusted line was derived by applying a power multiplier to the red curve for better visual comparison of the three profiles. The black line is the reference for the inertial subrange slope for turbulence spectra ($f^{-5/3}$).

## 5 Discussion and Conclusion

We have presented the application of a novel measurement and analysis technique using high speed infrared image acquisition and thermal image turbulent velocimetry. We have also shown a cross evaluation between the Thermal Image Velocimetry (TIV) and Image Segmentation (IS) methods. The TIV was used to derive the advection speed of thermal anomalies within the flaming zone, while the IS method was used to derive flaming parcel advection speeds that represented clusters of thermal anomalies from within the flaming zone. Both methods resulted in similar values despite their different approaches. The TIV method is preferable to the IS due to its ability for resolving the temporal and spatial turbulence scales. Previous research burns that used tower based sonic anemometer measurements for wind driven low intensity grass fires discussed the potential role of overlying turbulent wind velocity on fire behaviour (Clements et al., 2016; Ottmar et al., 2016). With thermal image turbulent velocimetry, it is now possible to characterize the spatial turbulence heterogeneity associated with atmospheric-surface interactions.

The nature of the frame-to-frame calculations of the TIV allowed for resolving turbulent perturbations at the camera's acquisition frame rate speed of 60 fps. The mean TIV-derived advection speeds from within the flaming zone for EE3 was less than the overlying wind speeds measured at 1.6m AGL (Figure 8a). The number distribution profile between the observed 1.6m wind speeds and TIV values was similar. We note that independently measured flame heights were placed between 1m and 2m for these burns placing the 1.6m sonic in or near the flaming zone. The difference between the TIV-derived advection speed and the 1.6m wind speed may be due to the observed LWIR closer to the surface.

Results from thermal image turbulent velocimetry should be analysed with care as the radiometric emission received by the camera sensors could involve multiple combustion sources from gases, fuel, ground and flames. Electromagnetic radiation is emitted by any substance that has a temperature above absolute zero, therefore the measurement of the brightness temperature of the flaming zone can be problematic as the fire chemical process discharges gases with reactive chemical species and smoke with different emissivity signatures spanning the long wave spectrum in use. The path between the emitting flame and the camera sensors has to be clear of any other emitting substances, which is hard to achieve in a field experiment. As a result, it is essential to describe the limitation of the measurement method of brightness temperature (Tb) and understand what dimensional components of the flaming zone we are measuring.

Emission of burning solid fuel and hot gases from the flame cannot be distin-

guished in the imagery, and the latter's grey body emissivity varies from 0.1 to 0.9 depending on combustion characteristics as flame depth and gas composition (Boulet et al., 2011; Johnston et al., 2014). Parent et al. (2010) carried out laboratory experiments of burning vegetation and recorded multispectral radiation intensity using filters installed on a LWIR camera and a spectrometer. It was found that the source of electromagnetic radiation can vary from the burning vegetation levels where soot emission is predominant following the Plank's law, through the flame lower heights where $H_2O$ vapor is dominant at ~7.8 microns, to flame mid to high levels where $CO_2$ is dominant at ~4.4 microns. Parent et al. (2010) concluded that the grey body emissivity varies between 0.8 close to the burning vegetation to around 0.3 for the flame. The LWIR camera used for this study has a broadband infrared spectrum between 7.7 to 9.3 microns and therefore we estimate that the highest radiation intensity values, and thus the Tb pixel values, are more likely to originate from the emitted radiation from soot particles and $H_2O$ vapor near the combusting fuels.

Further limitations can be attributed to the field of view, which was oblique for these experiments. Due to the oblique field of view, and the estimated velocimetry at the near-fuel levels, we cannot confidently suggest that the thermal image velocity results represent the true velocities parallel and perpendicular to the advancing fire line. The results are more likely to represent a spatial integral velocity scale of the 3-dimensional flame parcel targets.

The presented measurement and analysis technique is useful for analysing coherent flame parcel motion in field-scale fires that might be responsible for non-steady fuel heating. This phenomena was previously observed in controlled laboratory studies (Finney et al., 2015) and Tang et al. (2019) suggested that intermittent fuel heating frequency in wind driven fires is proportional to the ratio of Froude number (wind momentum allowing flame forward pulsation) and fire's heat release (allowing flame upward pulsation). Observations of forest crown fires suggest that coherent ambient wind gusts, possibly resulting from the interaction of the fire buoyancy and ambient atmospheric turbulence, can induce a variance in fire spread rate in the order of tens of seconds and tens of meters (Stocks et al., 2004; Taylor et al., 2004). As a result, it is crucial to be able to measure atmospheric-flame-fuel interactions in a spatially resolved manner. High speed infrared cameras coupled with a thermal image velocity algorithm can provide a useful tool for meeting this objective.

This work presented the first verification of the application of time-sequential thermography for studying fire-atmospheric turbulence interactions at a field-scale. In particular, the technique can be used to find and track the coherent flame parcel motions responsible for fuel convective heating and for relating the non-steady speed of flame parcels within the flaming zone to the turbulence perturbations in the overlying atmosphere. The TIV algorithm is available as an open-source toolkit (Schumacher, 2021).

Acknowledgments, Samples, and Data

We would like to give a special thanks to all field support teams including technical and general staff. We also thank landowner for their various contributions leading to the success of the field campaigns. University of Canterbury atmospheric research team would like to acknowledge the very thoughtful, well organized, and proactive support we have received from all the volunteering firefighting crew. The success of our experiments and the safety of our science crew can only be partially attributed to our design but greatly attributed to the safe and well-executed plan from the volunteer crew. A special thanks to the Scion field crew: David Glogoski, Max Novoselov, Richard Parker, Brooke O'Connor, Emma Percy, and Ilze Pretorius. This research was co-funded by Ministry of Business, Innovation and Employment (MBIE), New Zealand, grant number CO4X1603 entitled "Preparing New Zealand for Extreme Fire" and by the Royal Society of New Zealand grant number RDF-UOC1701. All data used for this anlaysis will become available at https://figshare.com.

References

Beare, R., Chen, J., Adamson, C. L., Silk, T., Thompson, D. K., Yang, J. Y. M., et al. (2013). Brain extraction using the watershed transform from markers. *Frontiers in Neuroinformatics*, *7*. https://doi.org/10.3389/fninf.2013.00032Blender Online. (2018). *Blender - a 3D modelling and rendering package*. Stichting Blender Foundation, Amsterdam. Retrieved from http://www.blender.orgBoulet, P., Parent, G., Acem, Z., Kaiss, A., Billaud, Y., Porterie, B., et al. (2011, April 7). Experimental Investigation of Radiation Emitted by Optically Thin to Optically Thick Wildland Flames [Research Article]. https://doi.org/10.1155/2011/137437Clark, T. L., Radke, L., Coen, J., & Middleton, D. (1999). Analysis of Small-Scale Convective Dynamics in a Crown Fire Using Infrared Video Camera Imagery. *Journal of Applied Meteorology and Climatology*, *38*(10), 1401–1420. https://doi.org/10.1175/1520-0450(1999)038<1401:AOSSCD>2.0.CO;2Clements, C. B., Zhong, S., Goodrick, S., Li, J., Potter, B. E., Bian, X., et al. (2007). Observing the Dynamics of Wildland Grass Fires: FireFlux—A Field Validation Experiment. *Bulletin of the American Meteorological Society*, *88*(9), 1369–1382. https://doi.org/10.1175/BAMS-88-9-1369Clements, C. B., Zhong, S., Bian, X., Heilman, W. E., & Byun, D. W. (2008). First observations of turbulence generated by grass fires. *Journal of Geophysical Research: Atmospheres*, *113*(D22). https://doi.org/10.1029/2008JD010014Clements, C. B., Lareau, N. P., Seto, D., Contezac, J., Davis, B., Teske, C., et al. (2016). Fire weather conditions and fire–atmosphere interactions observed during low-intensity prescribed fires – RxCADRE 2012. *International Journal of Wildland Fire*, *25*(1), 90–101. https://doi.org/10.1071/WF14173Coen, J., Mahalingam, S., & Daily, J. (2004). Infrared Imagery of Crown-Fire Dynamics during FROSTFIRE. *Journal of Applied Meteorology and Climatology*, *43*(9), 1241–1259. https://doi.org/10.1175/1520-0450(2004)043<1241:IIOCDD>2.0.CO;2Community, B. O. (2018). *Blender - a 3D modelling and rendering package* (manual). Stichting Blender Foundation, Amsterdam. Retrieved from http://www.blender.orgCram, D., Hatch, C. E., Tyler, S., & Ochoa, C. (2016). Use of Distributed Tempera-

ture Sensing Technology to Characterize Fire Behavior. *Sensors*, *16*(10), 1712. https://doi.org/10.3390/s16101712De Temmerman, P.-J., Verleysen, E., Lammertyn, J., & Mast, J. (2014). Semi-automatic size measurement of primary particles in aggregated nanomaterials by transmission electron microscopy. *Powder Technology*, *261*, 191–200. https://doi.org/10.1016/j.powtec.2014.04.040Finney, M., Cohen, J. D., Forthofer, J. M., McAllister, S. S., Gollner, M. J., Gorham, D. J., et al. (2015). Role of buoyant flame dynamics in wildfire spread. *Proceedings of the National Academy of Sciences*, *112*(32), 9833–9838. https://doi.org/10.1073/pnas.1504498112Finney, M., Pearce, G., Strand, T., Katurji, M., & Clements, C. (2018). *New Zealand prescribed fire experiments to test convective heat transfer in wildland fires* (pp. 1288–1292). Coimbra: Imprensa da Universidade de Coimbra. https://doi.org/10.14195/978-989-26-16-506_160Garai, A., & Kleissl, J. (2013). Interaction between coherent structures and surface temperature and its effect on ground heat flux in an unstably stratified boundary layer. *Journal of Turbulence*, *14*(8), 1–23. https://doi.org/10.1080/14685248.2013.806812Heilman, W. E., Bian, X., Clark, K. L., & Zhong, S. (2019). Observations of Turbulent Heat and Momentum Fluxes during Wildland Fires in Forested Environments. *Journal of Applied Meteorology and Climatology*, *58*(4), 813–829. https://doi.org/10.1175/JAMC-D-18-0199.1Hess, R. (2013). *Blender Foundations: The Essential Guide to Learning Blender 2.5*. Taylor & Francis.Hua, L., & Shao, G. (2017). The progress of operational forest fire monitoring with infrared remote sensing. *Journal of Forestry Research*, *28*(2), 215–229. https://doi.org/10.1007/s11676-016-0361-8Hudak, A. T., Dickinson, M. B., Bright, B. C., Kremens, R. L., Loudermilk, E. L., O'Brien, J. J., et al. (2016). Measurements relating fire radiative energy density and surface fuel consumption – RxCADRE 2011 and 2012. *International Journal of Wildland Fire*, *25*(1), 25–37. https://doi.org/10.1071/WF14159Inagaki, A., Kanda, M., Onomura, S., & Kumemura, H. (2013). Thermal Image Velocimetry. *Boundary-Layer Meteorology*, *149*(1), 1–18. https://doi.org/10.1007/s10546-013-9832-zJohnston, J. M., Wooster, M. J., & Lynham, T. J. (2014). Experimental confirmation of the MWIR and LWIR grey body assumption for vegetation fire flame emissivity. *International Journal of Wildland Fire*, *23*(4), 463–479. https://doi.org/10.1071/WF12197Katurji, M., Zawar-Reza, P., & Zhong, S. (2013). Surface layer response to topographic solar shading in Antarctica's dry valleys: SURFACE LAYER RESPONSE TO SOLAR SHADING. *Journal of Geophysical Research: Atmospheres*, *118*(22), 12,332-12,344. https://doi.org/10.1002/2013JD020530Mazzeo, G., Marchese, F., Filizzola, C., Pergola, N., & Tramutoli, V. (2007). A Multi-temporal Robust Satellite Technique (RST) for Forest Fire Detection. In *2007 International Workshop on the Analysis of Multi-temporal Remote Sensing Images* (pp. 1–6). https://doi.org/10.1109/MULTITEMP.2007.4293060McRae, D. J., Jin, J.-Z., Conard, S. G., Sukhinin, A. I., Ivanova, G. A., & Blake, T. W. (2005). Infrared characterization of fine-scale variability in behavior of boreal forest fires. *Canadian Journal of Forest Research*, *35*(9), 2194–2206. https://doi.org/10.1139/x05-096Morvan, D. (2011). Physical Phenomena and

Length Scales Governing the Behaviour of Wildfires: A Case for Physical Modelling. *Fire Technology*, *47*(2), 437–460. https://doi.org/10.1007/s10694-010-0160-2Najman, L., & Schmitt, M. (1994). Watershed of a continuous function. *Signal Processing*, *38*(1), 99–112. https://doi.org/10.1016/0165-1684(94)90059-0O'Brien, J. J., Loudermilk, E. L., Hornsby, B., Hudak, A. T., Bright, B. C., Dickinson, M. B., et al. (2016). High-resolution infrared thermography for capturing wildland fire behaviour: RxCADRE 2012. *International Journal of Wildland Fire*, *25*(1), 62–75. https://doi.org/10.1071/WF14165Ottmar, R. D., Hiers, J. K., Butler, B. W., Clements, C. B., Dickinson, M. B., Hudak, A. T., et al. (2016). Measurements, datasets and preliminary results from the RxCADRE project – 2008, 2011 and 2012. *International Journal of Wildland Fire*, *25*(1), 1–9. https://doi.org/10.1071/WF14161Parent, G., Acem, Z., Lechêne, S., & Boulet, P. (2010). Measurement of infrared radiation emitted by the flame of a vegetation fire. *International Journal of Thermal Sciences*, *49*(3), 555–562. https://doi.org/10.1016/j.ijthermalsci.2009.08.006Schumacher, B. (2021). ATIV: A-tiv starting release (Version v0.1). Zenodo. https://doi.org/10.5281/zenodo.4741550Schumacher, B., Katurji, M., Zhang, J., Stiperski, I., & Dunker, C. (2019). Evolution of micrometeorological observations: Instantaneous spatial and temporal surface wind velocity from thermal image processing. GeoComputation 2019.Seto, D., Clements, C. B., & Heilman, W. E. (2013). Turbulence spectra measured during fire front passage. *Agricultural and Forest Meteorology*, *169*, 195–210. https://doi.org/10.1016/j.agrformet.2012.09.015Seto, D., Strand, T. M., Clements, C. B., Thistle, H., & Mickler, R. (2014). Wind and plume thermodynamic structures during low-intensity subcanopy fires. *Agricultural and Forest Meteorology*, *198–199*, 53–61. https://doi.org/10.1016/j.agrformet.2014.07.006Stocks, B. J., Alexander, M. E., Wotton, B. M., Stefner, C. N., Flannigan, M. D., Taylor, S. W., et al. (2004). Crown fire behaviour in a northern jack pine - black spruce forest. *Canadian Journal of Forest Research*, *34*(8), 1548–1560. https://doi.org/10.1139/x04-054Stull, R. B. (2012). *An Introduction to Boundary Layer Meteorology*. Springer Science & Business Media.Sullivan, A. L. (2017a). Inside the Inferno: Fundamental Processes of Wildland Fire Behaviour: Part 1: Combustion Chemistry and Heat Release. *Current Forestry Reports*, *3*(2), 132–149. https://doi.org/10.1007/s40725-017-0057-0Sullivan, A. L. (2017b). Inside the Inferno: Fundamental Processes of Wildland Fire Behaviour: Part 2: Heat Transfer and Interactions. *Current Forestry Reports*, *3*(2), 150–171. https://doi.org/10.1007/s40725-017-0058-zTang, W., Finney, M., McAllister, S., & Gollner, M. (2019). An Experimental Study of Intermittent Heating Frequencies From Wind-Driven Flames. *Frontiers in Mechanical Engineering*, *5*. https://doi.org/10.3389/fmech.2019.00034Tangney, R., Issa, N. A., Merritt, D. J., Callow, J. N., & Miller, B. P. (2018). A method for extensive spatiotemporal assessment of soil temperatures during an experimental fire using distributed temperature sensing in optical fibre. *International Journal of Wildland Fire*, *27*(2), 135–140. https://doi.org/10.1071/WF17107Taylor, S. W., Wotton, B. M., Alexander, M. E., & Dalrymple, G. N. (2004). Variation in wind and crown fire behaviour in a northern jack pine - black spruce forest. *Canadian Journal of*

*Forest Research*, *34*(8), 1561–1576. https://doi.org/10.1139/x04-116Vickers, D., & Mahrt, L. (1997). Quality Control and Flux Sampling Problems for Tower and Aircraft Data. *Journal of Atmospheric and Oceanic Technology*, *14*(3), 512–526. https://doi.org/10.1175/1520-0426(1997)014<0512:QCAFSP>2.0.CO;2Welch, P. (1967). The use of fast Fourier transform for the estimation of power spectra: A method based on time averaging over short, modified periodograms. *IEEE Transactions on Audio and Electroacoustics*, *15*(2), 70–73. https://doi.org/10.1109/TAU.1967.1161901Wilczak, J. M., Oncley, S. P., & Stage, S. A. (2001). Sonic Anemometer Tilt Correction Algorithms. *Boundary-Layer Meteorology*, *99*(1), 127–150. https://doi.org/10.1023/A:1018966204465